# Carbon Stars and other Luminous Stellar Populations in M33

J.F. Rowe[1], H.B. Richer, J.P. Brewer[1]
University of British Columbia
6224 Agricultural Road, Vancouver, BC, V6T 1Z1
rowe@astro.ubc.ca,richer@astro.ubc.ca,jbrewer@bcit.ca

D.R. Crabtree[1]
Dominion Astrophysical Observatory, Herzberg Institute of Astrophysics, National Research Council
5071 W. Saanich Road, Victoria, BC, V8X 4M6
dennis.crabtree@nrc.ca

## ABSTRACT

The M33 galaxy is a nearby, relatively metal-poor, late-type spiral. Its proximity and almost face-on inclination means that it projects over a large area on the sky, making it an ideal candidate for wide-field CCD mosaic imaging. Photometry was obtained for more than $10^6$ stars covering a $74' \times 56'$ field centered on M33. Main sequence (MS), supergiant branch (SGB), red giant branch (RGB) and asymptotic giant branch (AGB) populations are identified and classified based on broad-band $V$ and $I$ photometry. Narrow-band filters are used to measure spectral features allowing the AGB population to be further divided into C and M-star types. The galactic structure of M33 is examined using star counts, colour-colour and colour-magnitude selected stellar populations. We use the C to M-star ratio to investigate the metallicity gradient in the disk of M33. The C/M-star ratio is found to increase and then flatten with increasing galactocentric radius in agreement with viscous disk formation models. The C-star luminosity function is found to be similar to M31 and the SMC, suggesting that C-stars should be useful distance indicators. The "spectacular arcs of carbon stars" in M33 postulated recently by Block et al. (2004) are found in our work to be simply an extension of M33's disk.

*Subject headings:* stars: carbon stars – galaxy: M33 – galaxy: stellar populations

## 1. Introduction

Carbon-star (C-star) production is caused when deep stellar convection dredges up material created by nuclear fusion processes. Whether a star is a C-star or M-star depends on the C/O ratio in its photosphere. If a star is formed from initially metal-poor material in the original protostellar cloud then less carbon is required to alter the surface chemistry from oxygen dominated (C/O $<$ 1) to carbon dominated (C/O $>$ 1). Photospheric chemistry is dominated by the production of CO molecules. An over-abundance of carbon leads to molecules such as CN being formed, whereas an over-abundance of oxygen leads to production of molecules such as TiO. An AGB star initially has an oxygen dominated photosphere, inhibiting the formation of CN as any carbon primarily forms CO. When a star undergoes dredge up, carbon rich material mixes into the photosphere. If there is initially a low oxygen abundance in the star then little carbon is needed to transform it from an M-star into a C-star. Thus, the ratio of the number of C-stars to M-stars will depend on the initial metallicity of the system, and observations support the idea that higher C/M ratios occur in lower metallicity systems and galaxies (Blanco & McCarthy (1983); Richer, Pritchet & Crabtree (1985a); Cook, Aaronson & Norris (1986); Mould & Aaronson (1986); Aaronson & Olszewski (1987); Brewer et al. (1995); Albert, Demers & Kunkel (2000)). The observed correlation spans 4 dex in C/M and 1.5 dex in [Fe/H] (Groenewegen 2002) and holds regardless of the galaxy morphology or star formation history. This provides a method to measure the metallicity distribution within a galaxy as only age and metallicity appear to have a strong effect on the C/M-star ratio.

[1]Visiting Astronomer, Canada-France-Hawaii Telescope (CFHT), operated by the National Research Council of Canada, le Centre National de la Recherche Scientifique de France, and the University of Hawaii

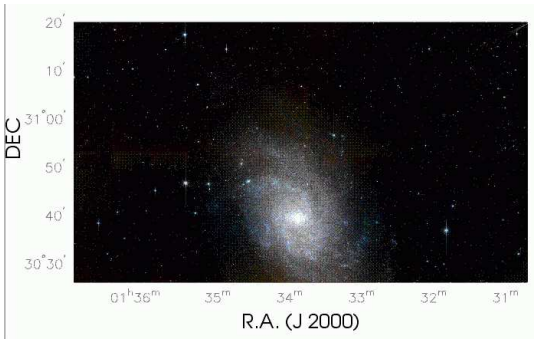


Fig. 1.— M33 mosaic V-band image constructed from the CFHT images and covering the entire area of the present survey.

Located in the Triangulum constellation, M33, also known as the Triangulum Galaxy, is a late-type spiral located approximately 840 kpc away. A V-band image using data from this work is shown in Figure 1. M33 is substanially smaller in size and mass than both M31 and the Milky Way and is an interesting target to study as its AGB/RGB stellar content is easily resolved in 4m class telescopes. In contrast to M31, M33's lack of nearby dwarf companions provides it with an almost isolated environment.

AGB stars are members of intermediate aged (1-10 Gyr) stellar populations and represent a relaxed subsystem in galaxies (Nowotny et al. 2001). This means that AGB stars uniquely record the star formation history of the galaxy at intermediate ages as well as sampling its history of minor mergers. By observing M33 to large galactocentric distances we can examine the underlying stellar population to see if there is evidence for recent tidal interactions. For example the newly discovered tidal ring that appears to surround the Milky Way was identified through observations of an F-star overabundance (Newberg et al. (2002); Ibata et al. (2003)).

Using the C/M-star ratio one can trace metallicity variations in a galaxy. Zaritsky's (Zaritsky 1992) star-forming viscous disk models predict a change in the slope of the metallicity gradient at the radius where the rotation curve flattens. The current data set allows us to measure the metallicity gradient of M33 as a function of galactocentric radius, thus allowing tests of galaxy formation and evolution models to be made.

### 1.1. C-star Classification

In order to distinguish C and M-type AGB stars, groups led by Richer (Richer et al. (1984); Richer, Pritchet & Crabtree (1985a); Richer & Crabtree (1985b); Pritchet et al. (1987); Hudon et al.1989 (1989); Richer et al. (1990)) and Aaronson (Aaronson et al. (1984), Cook, Aaronson & Norris (1986)) developed a four band photometric system (FBPS) to classify AGB stars.

The FBPS uses two narrow-band filters to provide low-resolution spectral information and two broad-band filters for temperature information. The filters used are listed in Table 1. A C-star spectrum will have CN bands, whereas an M-star is dominated by oxide bands such as $H_2O$ and TiO. The CN and TiO filters were developed to measure the CN and TiO molecular band strengths. Figure 11 of Brewer et al. (1996) illustrates spectra of a C-star, an M-star and an A-star and demonstrates how the filters easily discriminate between the three. A C-star will have strong absorption in the CN filter and when compared to the magnitude measured in TiO will produce a positive CN−TiO index. An M-star will produce a negative CN−TiO index, as it will exhibit strong absorption from TiO. An A-star will produce a CN−TiO index of approximately zero. In the study of Brewer et al. (1996) the validity of the system was confirmed by spectroscopic observations.

The FBPS allows large areas to be quickly surveyed by direct imaging, providing simultaneous measurements of all stars in the field of view. This is in contrast to spectroscopic observations which are limited to a relatively narrow field of view, small numbers of potential targets and longer integration times. The FBPS is also advantageous as it will work in fields too crowded for grisms. Spectroscopic survey strategies applied to the LMC (Blanco et al. (1980), Blanco & McCarthy (1983)) would not work in the present case on account of the faintness and crowding of M33's stars. A spectroscopic survey of all potential AGB stars in M33 for the purpose of classification is unfeasible. Using the FBPS, stars can be quickly classified and targeted for follow up spectroscopic studies.

## 2. Observations

Multiband photometric data were collected on October 30 and 31, 1999 and December 3 and 4, 2000, with the 3.58 m Canada-France-Hawaii Telescope (CFHT). The detector used was the CFH12k mosaic CCD camera which employs 12 MIT/LL CCID20 CCDs to provide an effective size of 12 228×8192 pixels. The camera is po-

sitioned at prime focus, has a pixel size of 15 microns, a plate scale of $0\farcs206$ /pixel and $42' \times 28'$ field of view (approximately 1.5 times the size of the full Moon).

The centres of the four fields in M33 that were observed are listed in Table 2. The total observed area covered by the 4 fields is $80' \times 50'$. An observing log is given in Table 3.

## 3. Data Reduction

The science images required correction of bad pixels, overscan and bias subtraction and flat-fielding. These operations were completed using the MSCRED package in IRAF[2].

Much of the CFH12k is free of defects, such as bad columns and hot pixels, but some CCDs show significant cosmetic flaws, such as CCD05 where approximately 30% of the CCD pixels are defective. Defective regions often show a non-linear response to the number of incident photons. For CFH12k, the number of ADUs per pixel at which non-linearity becomes significant is different for each CCD and ranges from 51k to 65k. Bad pixels and columns can be treated in two ways. The first is to ignore them in the reduction, the second is to interpolate over these pixels using surrounding pixels. The general approach taken in this work is to simply ignore bad pixels, especially since the images are dithered so chances are good that every part of the target will be observed at least once. Only in very specific cases do we apply a correction to bad pixels, which we will describe in §3.2. The broad-band data (obtained October, 1999) and narrow-band data (obtained December, 2000) were reduced in different ways as described below.

### 3.1. Narrow-band Data Processing

After bias corrections, gain differences across the CCD were corrected for by combining twilight flats for each filter. When combining frames, a 3 sigma clipping criterion (in MSCRED.COMBINE) is used to eliminate high and low pixel values. This works well for the sharp bright centres of stars' PSFs, but the extended wings are too faint to be excluded. To overcome this problem, a star's PSF is used as a tracer to reject all pixels within a specified radius. For CFH12k, a radius of 15 pixels was found to work well from visual examination of the images.

[2]Image Reduction and Analysis Facility (IRAF), a software package distributed by the National Optical Astronomy Observatories (NOAO)

### 3.2. Broad-band Data Processing

The flat-fields for the broad-band data set suffer from a strong, variable, scattered light pattern. Flat-fielding with these images introduced a 20% response error as a smooth gradient. The scattered light signal was also found to dramatically change with each flat-field image. This effect meant that when the images were averaged together, sigma clip routines to remove stars failed as it was impossible to scale each image to a uniform level so that deviant pixel values could be reliably removed. To fix this problem each flat-field image was heavily smoothed with a $500 \times 500$ pixel mean boxcar filter leaving behind the slowly varying background. Subtracting this signal away from the original flat-field image leaves an image containing the pixel-to-pixel sensitivity changes and objects such as stars and cosmic rays. A bad pixel mask was used to identify and correct the defects with interpolation from nearby pixels.

The residual images from subtracting the smoothed flat-field images were averaged using a sigma clipping algorithm to reject pixels affected by stars or cosmic rays. This flat-field corrects pixel-to-pixel sensitivity differences but failed to remove the overall gradient. This instrumental signature was removed by using the science images themselves. It was assumed that the individual CCD fields on the mosaic, which were farthest from the centre of the galaxy and hence least contaminated by stars, should be completely flat. The assumption of intrinsic flatness is justified as according to the NASA Extragalactic Database (NED) M33 reaches 25 mag arcsec$^{-2}$ in the B-filter at a major axis radius of $70\farcm8$. The ratio of the major axis to the minor axis is 1.70. The average B$-$V index of M33 reported by NED is 0.55 and the sky at Mauna Kea is approximately V=21.7 mag arcsec$^{-2}$ (Krisciunas 1990). Individual CCD images that are outside an ellipse centred on M33 with a major axis radius of $70\farcm$ and the same ellipticity as M33 were averaged to create a *super flat* which was then normalized to unity. Stars were removed from the individual images using PSF fits and also applying the same sigma clipping algorithm used for the creation of regular flat-fields. A minimum of 3 images per CCD were combined to create the super flat-field. Since this calibration is being used for the removal of a slowly changing gradient, the image was smoothed using a $3 \times 3$ mean boxcar. Subtraction of the smoothed image from the original showed a flat image consistent with the expected noise level. The flat-fielded science images were then divided by the super flat-field to remove the instrumental gradient.

### 3.3. Photometry

All stellar photometry was performed using the DAOPhot/ALLSTAR package (Stetson (1987), Stetson (1994)). As DAOPhot is unable to handle multi-extension FITS images each mosaic frame was split into its individual frames. This gave a total of 612 images which were all treated independently for the extraction of photometric data.

In order to account for geometric distortions in the PSFs, 150 stars were selected on each image and used to construct a quadratically varying PSF. The photometric measurements were made with ALLSTAR, which simultaneously fits groups of stars found close to each other on the frame with the PSF. Using photometry from each CCD chip, registration of the chips relative to one another was done with DAOMatch/DAOMaster. This worked well with each individual chip and a 20 parameter transformation was used to model the geometric distortions, so that the measured pixel positions of the stars on each CCD chip could be matched to other observations of the same field on the same chip. For example, for CCD01 in Field-2, there were 3 sets of observations in each of the four filters. These 12 images were then registered to match common objects for each field. Each observation was slightly offset from one another, meaning that some stars were observed on two adjacent detectors. Using these common observations, the complete photometric catalogue was pieced together, placing all objects on a common co-ordinate system as described in the next section.

### 3.4. Astrometric Registration

In order to identify common objects between adjacent CCDs the pixel co-ordinate system had to be transferred to J2000 co-ordinates. The rationale for this procedure is that DAOMatch/DAOMaster failed to converge to a proper registration solution, as less than 5% of the area of two chips overlapped from the dithered observations. When DAOMaster finds a transformation, it is only valid for the objects in common between the images. Extrapolation of the solution to adjacent CCDs would introduce large distortions. Instead, the pixel co-ordinate system for each CCD chip was first mapped to the J2000 co-ordinate system.

Common stars between this survey and the USNO-A2 astrometric catalogue were identified by using the MSCZERO and CCFIND IRAF commands found in the MSCRED and IMCOO packages. The CCMAP program was used to automatically cross-identify 100 common stars in each CCD frame by finding the brightest star within a 20×20-pixel search box. The success rate was approximately 75%, with a majority of failures due to catalogue stars located outside the imaged area. The CCMAP program was then used to compute a rough astrometric solution based on all cross-identifications, including incorrect ones, since the number of true matches dominates the list. These solutions had an RMS error of approximately $6''$. With this plate solution, the Starlink package GAIA was used to identify common stars between the two catalogues. The output from GAIA was input into CCMAP to compute an accurate plate solution. The average RMS error was reduced to $0\farcs5$ or approximately 2 pixels, which is about the internal accuracy of the USNO-A2 catalog. The entire photometric catalogue was then transformed onto the J2000 co-ordinate system.

This new catalogue was searched for duplicate objects that were imaged on adjacent CCDs. These objects were located by identifying the closest neighbour to each object and the closest objects to that neighbouring star. If two stars were found to be closer than $1.5''$ and their instrumental magnitudes differed by less than 0.1 magnitudes, then those stars were assumed to be the same and combined into a single entry.

### 3.5. Photometric Calibration

The master astrometric catalogue was corrected for zero-point instrumental magnitude offsets between each observation, chip and field. These values were calculated from the identification of common objects in the master catalogue. Figure 2 shows the calibration data for stars common to Field 1 and Field 2 for each filter. The lack of scatter, other than the expected photometric errors, confirms that the cross-identification of common objects works very well. The average error for all measured magitude offsets is approximately 0.01 magnitudes and the standard deviation from the fit for stars with an instrumental magnitude greater than 14 is approximately 0.02 magnitudes. This is also a measure of the quality of the flat-fielding using stars common to Field 1 and Field 2. If any gradients exist then one would observe a systematic offset in Figure 2 from flat-fielding errors. One potential problem is that the calibration of each chip is dependent only on adjacent chips, thus the offset will inherit errors from every other chip other than the CCD selected as the zero point reference. A CCD chip that is 5 CCDs away from the reference chip could suffer from a large (0.1 magnitude) systematic offset. This effect was monitored by plotting the colour magnitude diagram for the reference

chip overlaid with that for the CCD chip being corrected. Examination of the CMDs on opposite sides of the mosaic shows no difference greater than 0.05 magnitudes, which is the accuracy at which any offsets could be detected through the examination of colour-magnitude diagrams.

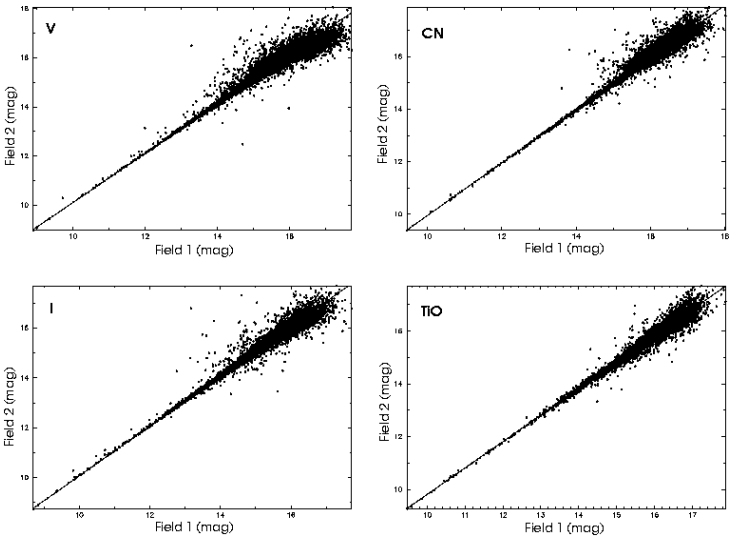


Fig. 2.— The photometric offsets between the instrumental magnitudes of Field 1 and Field 2 for each filter. Each field is identified with a subscript.

With all of the photometry set to a common instrumental photometric system, transformation to the standard system for the V and I filters was computed using data from the DIRECT project (Macri et al. 2001). Comparison of the two photometry data sets is shown in Figure 3. The scatter in this fit for stars brighter than V, I=12 is 0.03 and 0.08 magnitudes respectively. This is consistent with the internal magnitude calibration of the DIRECT project, as seen in Figure 9 of Macri et al. (2001). With errors this large, a reliable colour term could not be determined. Instead, only bright stars with a V−I colour less than 0.3 magnitudes were used to determine the zero-point offsets; otherwise the average colour terms for CFH12k from the online observer's manual were used. The adopted transformation equations are

$$\begin{aligned} V &= V_{\rm i} + 7.39 + 0.001(V_{\rm i} - I_{\rm i}) \\ I &= I_{\rm i} + 6.42 - 0.010(V_{\rm i} - I_{\rm i}) \end{aligned} \quad (1)$$

where $V_{\rm i}$ and $I_{\rm i}$ are the observed instrumental magnitudes.

Calibration of the TiO and CN magnitudes was much easier. It is expected that the CN−TiO measurements for stars not on the AGB, such as the MS should have CN−TiO≃0. These stars lack the strong TiO and CN absorption bands found in the cooler AGB stars and the TiO and CN filters lie on no strong absorption features. The TiO magnitudes were adjusted such that CN−TiO has an average of zero for stars with V−I less than 0.8. The true magnitude of a star observed in these filters is irrelevant, as only the difference between them provides a measurement for identification of C and M-stars.

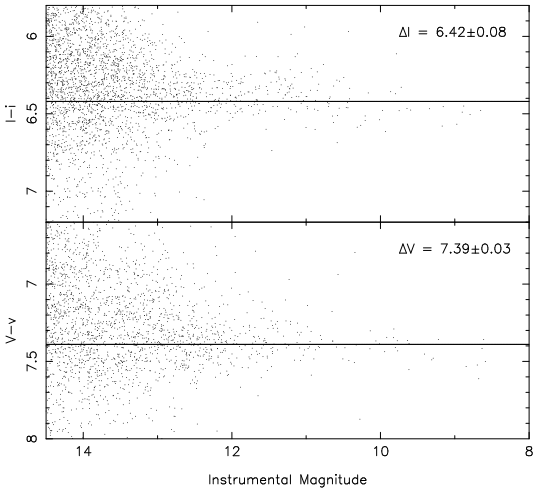


Fig. 3.— A comparison of CFHT instrumental photometry with the DIRECT project for the V and I filters. Uppercase letters refer to standards taken from the DIRECT project and lower case letter refer to the instrumental photometry from this study. Also shown is the zero point offset adopted for each filter.

### 3.6. Completeness Tests

Many aspects of this work involve relative counts of star types. When observing a large extended object such as a galaxy, the detected number of stars will vary from region to region due to properties of the galaxy and constraints due to instrumentation. In order to compare relative statistics across the galaxy the completeness needs to be known as a function of position.

Estimating detection limits due to the galaxy's structure requires understanding knowledge of the poorly understood dust extinction. Looking at Figure 1, or any B or V band image of M33, it is easy to identify extinction in spiral arms that is caused by dust. Star counts

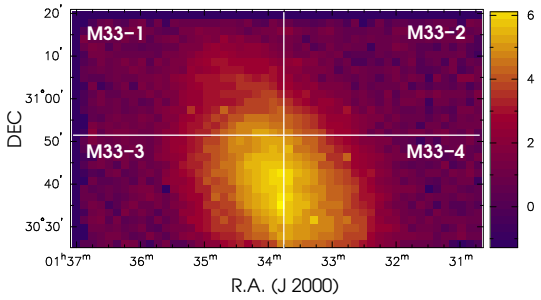


Fig. 4.— Spatial map of all observed stars with completeness corrections. The density scale is ln(number of stars per square arcsec). The approximate boundaries of each target field is also shown.

in dusty region will be lower as more stars will fall below the detection limits.

Detection limits due to instrumental constraints are primarily due to a lack of resolution. Detecting a star requires isolation of its PSF on an image. In very crowded fields it becomes impossible to separate each stellar component. It is possible to test the confusion limit through Monte-Carlo methods.

The Monte Carlo tests, now known as *addstar tests*, artificially add stars to a frame and attempt to recover them under the same conditions as the original photometry was obtained. Comparing the input star list to the recovered objects gives a measurement of detection limits and completeness due to instrumental effects. No information is gained about extinction due to dust. Addstar tests were performed using the DAOPhot and ALLSTAR packages, making use of the ADDSTAR routine. This routine uses the model PSF that was generated from the original photometry extraction to add artificial stars to the image. The star must be added with the same noise characteristics as a star of the same instrumental magnitude. If addstar tests are to be a valid estimation of the true completeness, then the test must not significantly alter the crowding statistics in the image when adding stars to it. The input stars must also have colour indices similar to the original stars in the image. Thus, the original photometry list is used to generate the artificial input stars.

We added 1000 stars per frame. This number appeared not to make even the most sparse fields (which contain just over 1000 stars) over-dense. Analysis of the sparse fields showed that 99.8% of stars added at 100 sigma level were recovered, adding confidence that our choice of adding 1000 stars per frame would not affect crowding statistics.

To generate the magnitude of an artifical star and its relative colour indices, binned colour-magnitude diagrams and colour-colour diagrams, also called Hess diagrams, (see §4.2 and §4.4) are used to determine the probability of generating stellar parameters. First a CN−TiO versus V−I diagram is binned by 0.1 mag. The number of stars in each bin is divided by the sum of all the bins to generate a probability. A random number between 0.000 and 1.000 is generated and bins are summed by row (V−I) then incremented in column (CN−TiO) until the sum of the bin is greater than the random number. This bin determines the CN−TiO and V−I indices of the artificial star. Next a CN versus CN−TiO normalized grid is used to determine the CN magnitude based on the corresponding CN−TiO column and likewise a V vs V−I grid was used to determine the corresponding V magnitude. The artificial CMDs generated in this manner appeared identical to the original data set. The artificial magnitudes were then transformed back to the instrumental magnitude system using the calibrations from §3.5. The generated number of C-stars was close to 100, as there is approximately 1 C-star for every 100 other types of star. Since C-star completeness tests is important in our analysis, the artificially generated star list was changed by taking the logarithmic value of each bin in the weighting grids before normalization. This places more weight on generating stars with small populations. Close to a hundred carbon stars were generated with this alteration, giving good statistics for completeness determinations.

There were 51 exposures between all four filters and there are 12 chips per exposure. The addstar test was run 10 times to obtain good statistics for the completeness of the entire stellar population. In total, $6.12 \times 10^6$ stars were added to the frames. Before stars were added to a frame, each CCD for the same field of view was registered using MONTAGE2 from the DAOPhot package to match star co-ordinates, using the plate solutions from §3.4 to aid in cross identification afterwards. Geometrically altering an image can introduce noise and artificial artifacts, but is minimized if the image is oversampled. The FWHM of a star should be greater than 2 pixels to

avoid registration artifacts. Under the best seeing conditions the FWHM was just under 3 pixels in our images. For each image the photometry steps from §3.3 were repeated.

The new photometry lists, containing the artificial stars, were matched to the artificial star catalogue, and completeness statistics were gathered. In Figure 5 the global completeness level is plotted as a function of position. The spatial scale is identical to Figure 1. One can see that each of the four pointings has a different completeness level, which is due to changing seeing conditions, and that Field 3 had more observations that any other field and hence detected fainter stars.

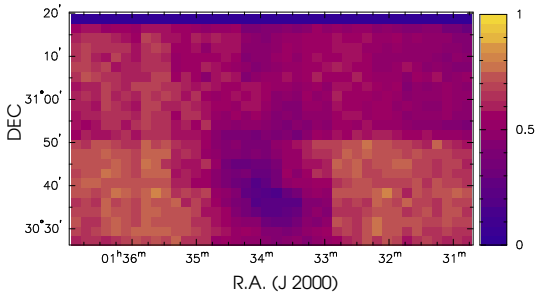


Fig. 5.— This figure shows the relative completeness for all observed regions. Field 3 (bottom left) has more observations than other regions, such as Field 2 (upper right) and has a higher completeness level.

## 4. Results

### 4.1. Star Counts

In Figure 4, the spatial distribution of stars appears relatively uniform. This is different from what is observed in star count distributions for M31, as presented in Figures 2 and 3 of Ferguson et al. (2002). M31, like the Milky Way, has dwarf spherical companions, and their presence can be detected by streams of stars sharing common orbits. In the Milky Way there is the Sagittarius Dwarf Galaxy, which is currently being sheared apart through gravitational interaction with our Galaxy. Mapping the spatial distribution of evolved stars, such as C-stars or RR Lyrae type variables (Vivas & Zinn 2002), reveals tidal tails from the Sagittarius Dwarf. Streams of star have also been observed emanating from globular clusters such as Pal 5 (Odenkirchen et al. 2001). Thus, if M33 has unseen companions their presence could be betrayed in a complete star map by selecting specific stellar populations.

Visual examination of the raw star map for M33 does not reveal any obvious perturbations. However, if accreted satellites have no luminous stellar component (White & Rees (1978) Dekel & Silk (1986)) their presence could be hidden in stellar density maps. A more detailed exercise is to examine distributions of specific stellar populations that represent different epochs of star formation, tracing the dynamical history of the galaxy through perturbations of its stellar population. To do this, we need to examine the colour-magnitude diagrams of M33 and identify relevant populations.

### 4.2. Colour-Magnitude Diagrams

In Figure 6, a calibrated colour-magnitude diagram (CMD) for I versus V−I is presented for stellar objects from our survey with errors in the colour term less that 0.05 mag. The MS, SGB, RGB and AGB are all visible. In Figure 6 the MS is seen as a strong vertical band between $-0.5 \lesssim$ V−I $\lesssim 0.35$. This represents young, luminous blue stars and provides a tracer of very recent star formation. Using Padova theoretical isochrones (Girardi et al. 2000) for a young stellar population (age $6.31 \times 10^7$ yr) and adopting a distance modulus of 24.64 (Freedman et al. 1991) gives a mass of approximately 5.8 $M_\odot$ at V=22 for a stellar population with Z=0.008. The large number of MS stars is no surprise, as the spiral arms in M33 are regions of active star formation.

The red SGB is seen as a band of stars extending to V $\simeq 19$, V−I $\simeq 2$ out from the RGB which is seen as a large clump centred at V $\simeq 22.5$ and V−I $\simeq 1.5$. The AGB population, where C-stars will be found, is the band of stars with V−I $\gtrsim 2$ and V $\lesssim 21$. Foreground contamination from Galactic stars is seen as a vertical sequence at V−I $\simeq 0.8$ extending up to V=15, the saturation limit of the detector. This CMD is a very useful tool for isolating specific stellar populations as will be seen in §4.3 and §4.5.

The distribution of stars on the CMDs is a result of star formation, stellar evolution and extinction. The effects of star formation and stellar evolution are observed through the presence of very young OB stars and older RGB and AGB stars. Extinction has the effect of blur-

ring the CMD by shifting observations dimmer and redward. Since the amount of extinction depends upon the line of sight, stars with the same intrinsic luminosity and colour can appear at different locations in the CMD.

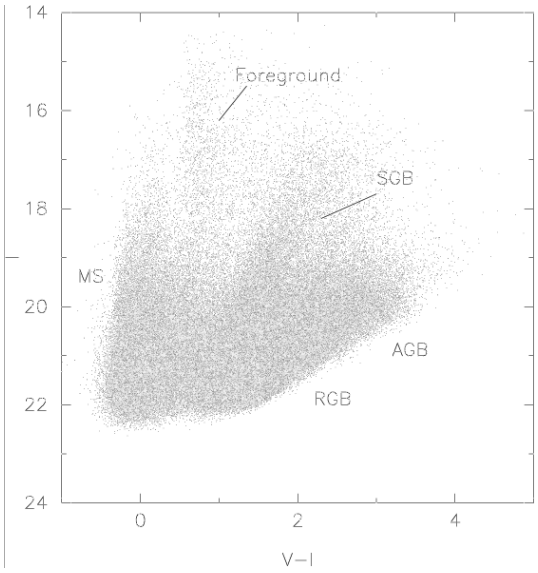


Fig. 6.— I, V−I colour magnitude diagram for stars with V−I errors less than 0.05 mag (choosen to allow various stellar populations to be easily perceived). The major stellar populations are indicated as described in the text.

### 4.3. CMD Selected Star Counts

The substructure of halos and disks of nearby galaxies contains clues about hierarchical galaxy formation. State-of-the-art simulations (Klypin et al. (1999), Moore et al. (1999)) show that accreted sub-halos last much longer than previously thought, with the central core lasting several tidal timescales (Hayashi & Navarro 2002), and several hundred cores could reside in galaxies like the Milky Way and M33.

Our survey data allows us to select specific stellar populations over most of the M33's disk. The observed MS reflects recent star formation since the MS lifetimes for the massive and luminous stars is short (under 1 Gyr). MS stars were chosen as stars with V−I colours less than 0.35 mag. The resulting distribution is shown in Figure 7. As should be expected, the spiral arm patterns seen in Figure 1 are also well traced by luminous MS stars. The bottom panel of Figure 7 is a binned map of MS stars with $15 < V < 22$ that has been completeness corrected using the data from §3.6. This map shows all MS stars with masses greater than $6M_{\odot}$ and the major spiral arms of the galaxy are well traced. The centre of M33 appears as a hole, as stellar crowding is too great to allow reliable detection of any stars in the region. The application of stellarity cuts eliminated all detections in this region of the galaxy.

The same exercise can be applied to the SGB population. SGB stars are identified by selecting all stars with a V−I colour greater than 1.2 and a V magnitude less than 21.75. Faint stars are excluded to avoid RGB stars at the base of the RGB clump. The distributions of SGB stars is shown in Figure 8. Like the MS stars, the SGB population is relatively young and will trace out stellar populations with ages less than about 1 Gyr. The SGB map suffers from foreground contamination by M-dwarfs, seen as a scatter of stars over all observed fields, but the galaxy is still identifiable. The SGB population is largest in areas containing the most MS stars. This occurs because both groups of stars have similar ages and the MS lifetimes are longer than stars found in the SGB phase. Both the SGB and MS maps (Figures 7 and 8) trace out a high density structure that almost encloses the centre of the galaxy. This feature starts on the east side of the galaxy extending south of the galaxy's centre and then to the west of the galaxy where it then sharply turns eastward toward the galaxy centre and then blends into two spiral arms that extend northward.

The spatial distribution of AGB stars is shown in Figure 9. The population shows a smooth distribution of stars compared to the clumpy distribution of MS stars. This is due to dispersion of the AGB population. M33 itself shows many localized regions of massive star birth, such as the gas complex NGC 604. Over time, new stellar associations will disperse. Thus, the distribution of MS stars will appear clumpier than that of AGB stars.

The AGB star map does not show any extended structure apart from gently tracing out the spiral arms. At semi-major radii larger than $30'$, the AGB population of M33 is lost due to foreground confusion from Galactic red dwarfs. Just as with MS stars, incompleteness is strongest towards the centre of M33, creating an apparent hole.

### 4.4. Colour-Colour Diagrams

The broad-band photometry can be combined with the narrow-band photometry to discriminate between spectral sub-types, namely C-stars and M-stars. Figure 10 shows the colour-colour diagram for the entire M33 field. The carbon stars, which have strong CN ab-

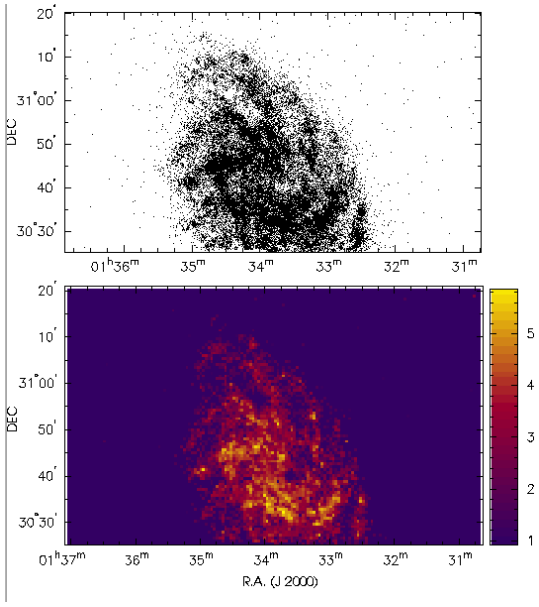


Fig. 7.— The surface density map of MS stars across the survey area. All stars with V−I < 0.35 are plotted. In the top panel the galaxy centre appears to have few MS stars because of incompleteness due to extreme stellar crowding. The bottom panel shows the binned surface density map for 15 < V < 22. This map has been completeness corrected. The density scale is ln(number of stars per square arcsec).

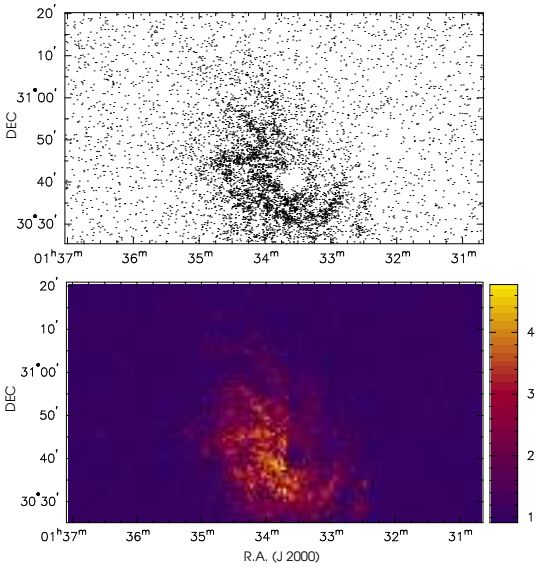


Fig. 8.— Surface density map of Super Giant stars across the survey area. All stars with V−I > 1.2 and V < 21.2 are plotted. The bottom panel shows the binned surface density map and has been completeness corrected. The density scale is ln(number of stars per square arcsec).

sorption bands appear as an isolated group with an average CN-TiO index of 0.5. The M-stars, with strong TiO absorption bands, tail-off from the RGB population at approximately V−I=2 towards redder colours or later spectral type. There is a difference of about 1 magnitude between the CN-TiO index values of C-stars and M-stars; the CN and TiO filters clearly do a good job at selecting AGB sub-types.

M31 has a distance modulus of 24.47 (Durrell et al. 2001) and M33 has a measured distance modulus of 24.64 (Freedman et al. 1991). The $1\sigma$ errors in the measurements are approximately $\pm$ 0.15, thus, to within $1\sigma$ M31 and M33 are at the same distance. To define the selection boxes for choosing M-stars and C-stars, the criteria of Brewer et al. (1996) for M31 are adopted. C-stars are identified with CN−TiO > 0.3 and M-stars with CN−TiO < −0.2 and both types must have V−I > 1.8. These were originally chosen by spectrally identifying C and M-stars and selecting colour values that encompassed C-stars without contamination (see Brewer et al. (1996) for details).

Figure 11 shows a colour-magnitude diagram for the 7936 C-stars selected using the adopted criteria. The completeness limit will be discussed later in this section.

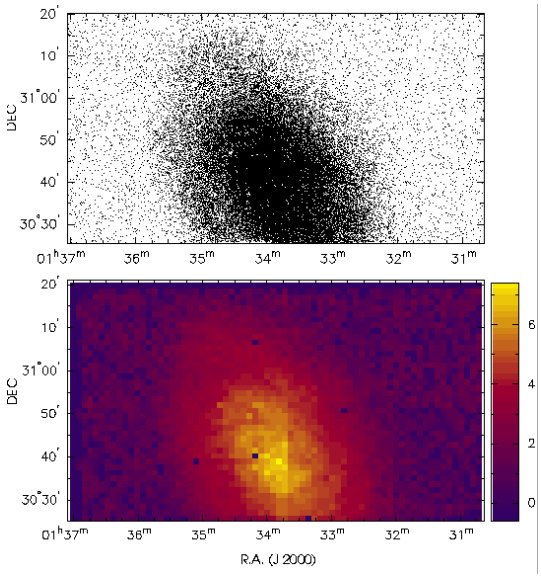


Fig. 9.— Surface density map of AGB stars across the survey area. All stars with V−I > 2.0 and 19 < I < 21 are plotted. There are instrumental artifacts towards the center of the galaxy due to incompleteness. The lower panel shows the binned surface density map. This map has been completeness corrected. The density scale is ln(number of stars per square arcsec).

As expected, these stars occupy the AGB branch location of the CMD. The foreground contamination of C-stars from the Milky Way is unimportant, the surface density being only 0.019 deg$^{-2}$ (Green 1992) down to V=18.

The M-star population will suffer strong contamination from the Milky Way. NGC 6822 (at b=−18°) was observed to have approximately 9000 foreground stars over a 28′×42′ field of view (Letarte et al. 2002). M33 (b=−31°), while at a higher Galactic latitude, will still suffer a substantial M-star foreground contamination (see §4.5). Contamination from non-AGB members within M33 is not a serious problem, as members of the RGB and SGB populations will not have strong CN or TiO absorption bands. However, choosing an I-band magnitude cut will limit foreground contamination and contamination from non-AGB stars in M33. Using Figure 11, C-stars and M-stars also have I magnitudes between 18.5 and 21. These values were chosen to enclose a majority of the detected C-stars, with out straying far below the 100% completeness limit. To quickly estimate the completeness limit in the I-band, the raw luminosity function, shown in Figure 12, was used. The number of stars rises approximately linearly towards fainter magnitudes, until approximately I=22 mag, when the number of objects quickly declines as the detection limit is reached.

### 4.5. Colour-Colour Diagram Selected Star Counts

As a continuation of §4.3 we can now examine the AGB stellar content of M33. Figure 13 and the top panel of Figure 14 show the spatial distribution of C-stars in M33. The distribution of C-stars traces out the extent of M33's disk well, as there is very little foreground contamination. Visual comparison of Figure 13 with the MS map in Figure 7 shows that the C-star distribution does exhibit some spiral structure. This is not unexpected, as the C-star population represents intermediate aged stars that were produced in spiral arms just like the current population of young stars. Their velocity dispersion as well as differential galactic rotation has slowly begun to smooth out the older population.

#### *4.5.1. Tidal Interactions*

There is no evidence of tidal disruption within the C-star population, neither is there indication of C-stars originating from a different system. This is in contrast to the claim of Block et al. (2004) who suggest that M33 displays "spectacular arcs of carbon stars" beyond 14′ from its nucleus. The lack of external interactions may be a reason why M33 displays beautiful *grand design* spiral

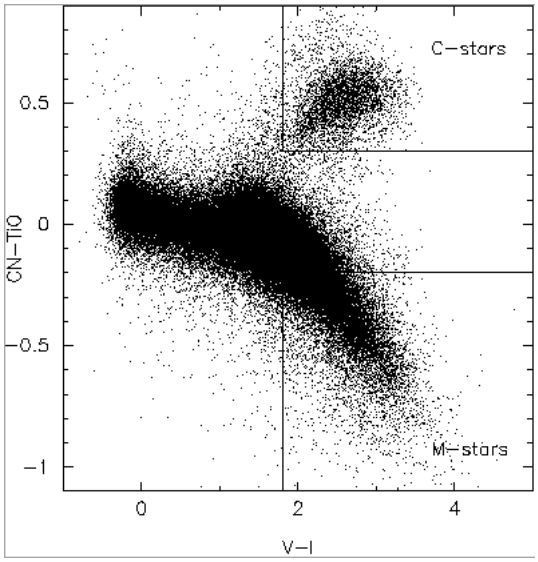


Fig. 10.— Colour-colour magnitude diagram for CN−TiO versus V−I for all stars with errors less than 0.05 magnitudes in CN−TiO and V−I. The C-stars and M-stars are clearly differentiated in this diagram. The few stars with V−I ¿ 1.8 and between the C and M-star region are likely S-stars.

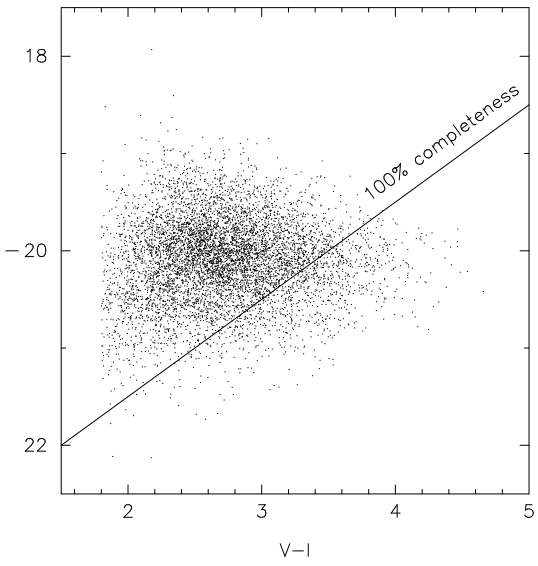


Fig. 11.— Colour-magnitude diagram for all C-stars. The 100% detection completeness limit is shown.

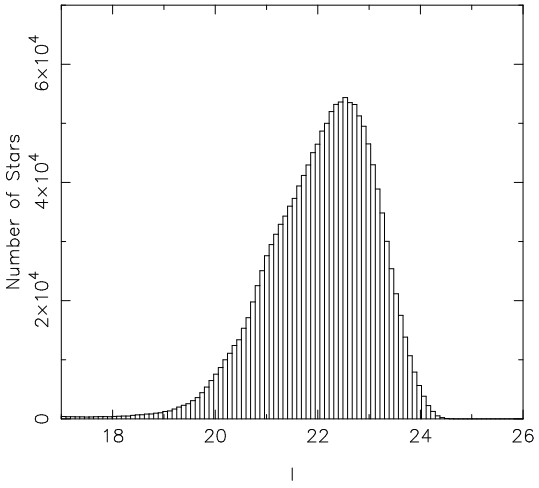


Fig. 12.— Luminosity function for all detected objects. The turnover at 22.5 mag gives an estimation of the completeness limit.

arms that can be traced from the outer most regions of the disk directly towards the center of the galaxy. The bottom panel in Figure 14 shows the corresponding M-star distribution. It is similar to the C-star distribution, except that foreground contamination, from Milky Way M-dwarfs, is stronger.

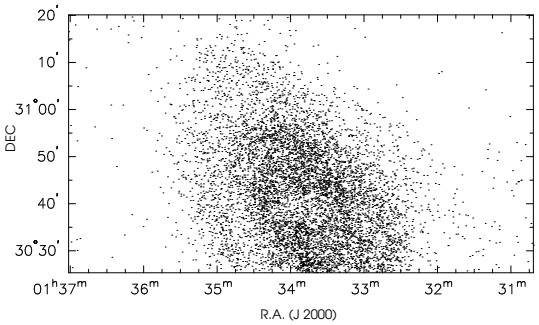


Fig. 13.— Spatial map of C-stars. As seen in previous star-maps, incompleteness is strongest towards the centre of the galaxy giving the appearance of a hole.

### *4.5.2. Radial Distributions*

The radial distribution of stars in a galaxy allows a quantitative measurement of the galaxy's morphology. To extract radial profiles from M33, its tilt must be taken into account. To do this, shape parameters for M33 from

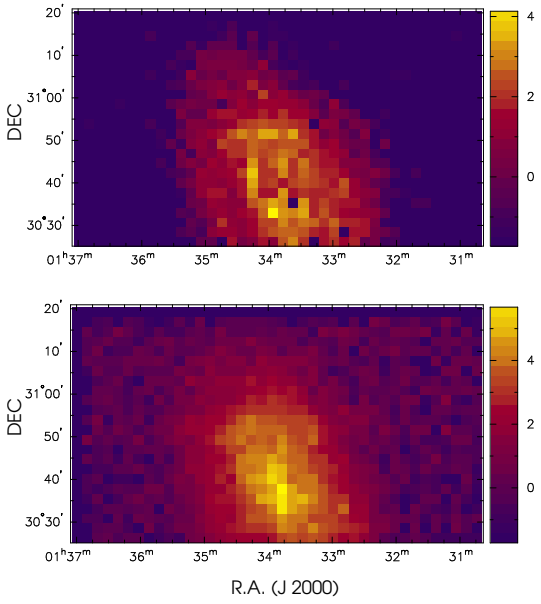


Fig. 14.— The top panel shows the binned surface density map of C-stars and the lower panel shows the M-stars. Both maps have been completeness corrected. The density scale is ln(number of stars per square arcsec).

the Third Reference Catalogue of Bright Galaxies (RC3) were obtained from the NASA Extragalactic Database (NED), specifically the length of the semi-major axis and the ratio of the semi-major axis to the semi-minor axis. If M33 was seen face on its shape would be a circle. Ellipses centred on M33 were constructed with different radii, and star counts were made for each radius using completeness corrected C and M-star counts. Figures 15 and 16 show the deprojected radial profile for M33 for C-stars and M-stars, respectively, in units of ln(number of stars per arcmin$^2$).

Examining the C-star profile, we see that it is flat from the centre of M33 out to 15′ and then the number density of stars decreases out to 50′. Here the slope changes again, and becomes flat out to approximately 70′ beyond which there are too few C-stars to provide useful statistics. The M-star profile is qualitatively similar to the C-star profile. The number density of M-stars decreases out to about 20′ from the centre of the galaxy, where there is a steepening of the slope and the distribution drops off. This feature can be seen in the lower panel of Figure 14 as a separation between the inner and outer disk in the distribution. At 45′, the foreground population of M-stars becomes dominant, reducing the slope of the M-star population out to the edge of the field of view.

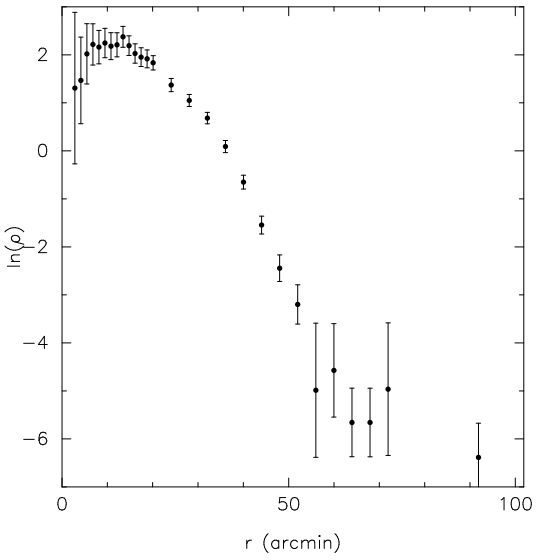


Fig. 15.— Stellar density profile for C-stars in M33. The units of density are ln(number of stars per arcmin$^2$).

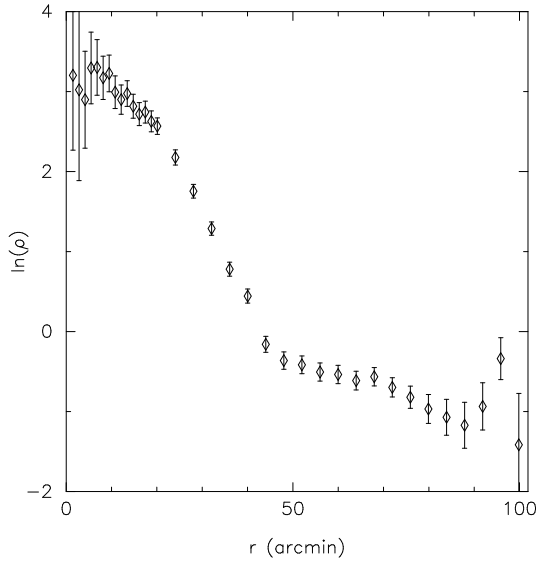


Fig. 16.— Stellar density profile for M-stars in M33. The units of density are ln(number of stars per arcmin$^2$).

### *4.5.3. Metallicity Gradients*

The time needed for a stellar population to produce the majority of its carbon stars is about 1 Gyr, thus for stellar populations older than this the C/M-ratio is independent of the star formation history (Mouhcine & Lançon 2003). Since the ratio of C-stars to M-stars is a tracer of metallicity, the C-star and M-star profiles can be converted into a completeness corrected C/M-ratio profile. Before this can be done, the foreground population of M-stars needs to be estimated. It is assumed that this population of M-stars is uniform across the field. The M-star profile is then used to estimate the foreground population. This was done by assuming that the M-star profile has a constant value beyond $25'$ obeying an exponential disk profile. The foreground M-star population was in this way estimated to be $0.50 \pm 0.03$ arcmin$^{-2}$. This gives approximately 2300 foreground M-stars over the field of view. As a check the foreground population can also be easily calculated by counting stars at the periphery of the image. All M-stars with an RA greater than $1^h\ 36^m$ were considered to be foreground M-stars as this area contains few C-stars. The completeness corrected stellar density of M-stars in this region was found to be $0.55 \pm 0.03$ arcmin$^{-2}$ consistent with our derived value. Figure 17 shows the C/M-ratio as a function of galactocentric radius. The ratio increases to a radius of $12'$ and then flattens for the outer disk regions. This result indicates that the metallicity of M33 is high in the centre and low in the outer parts of the disk, with a change in the gradient along the way. This is compatable with other metallicity gradient measurements (Vilchez et al. 1988).

These results are consistent with viscous disk formation models that predict exponential surface luminosity profiles of spiral galaxy disks (Zaritsky 1992). The rotation curves of spiral galaxies show solid body rotation in the inner parts of the disk and flat rotation curves in the outer part of the disk, where the rotation curve is dominated by dark matter. For solid body rotation there is no angular velocity difference between material at different radii, meaning that there is no viscous drag or turbulent diffusion. In the outer parts of the disk, the opposite is true with the production of radial gas flows. In galaxy formation models, negative abundance gradients are produced (Sommer-Larsen & Yoshii 1990), the evolutionary effect of rotation then smooths the metallicity gradient in the outer disk where the rotation curve is flat. Radial outflows will transfer metal-rich material into metal poor material, and vice versa with radial inflows. This produces a metallicity distribution with a change in slope where the rotation curve flattens. Examination of the 21cm rotation curve for M33 (Corbelli & Salucci 2000) reveals that, in fact, the rotation curve flattens around $10-15'$, consistent with our findings.

The current data set allow for a C/M-ratio map for M33. This completeness corrected map is shown in Figure 18. The increase in the C/M-ratio with increasing radius is apparent, as are two regions with a high C/M-ratio. The areas of enhanced C/M ratio are located in the regions where the arcs mentioned in Block et al. (2004) are to be found. The number of M-stars and C-stars drops towards the edge of the disk, thus the error in the C/M-star measurement will be higher in these regions. The second and third panel in Figure 18 show the associated error and the signal-to-noise ratio (S/N) for each region in the C/M-ratio map. The peak in the northern region of high C/M has a S/N less than 3 and its associated error in the ratio is approximately 0.35, making the detection of the peak with the bin size used somewhat uncertain. The same argument applies to the south-west region of the map.

To test whether the enhanced C/M-ratio regions are statistically significant, the S/N can be increased by increasing the bin size to avoid small number statistics. The C/M-ratio map was rebinned with an area four times greater. The north and southwest regions each have average C/M-ratios of 0.5 and $0.6 \pm 0.04$ respectively. Other

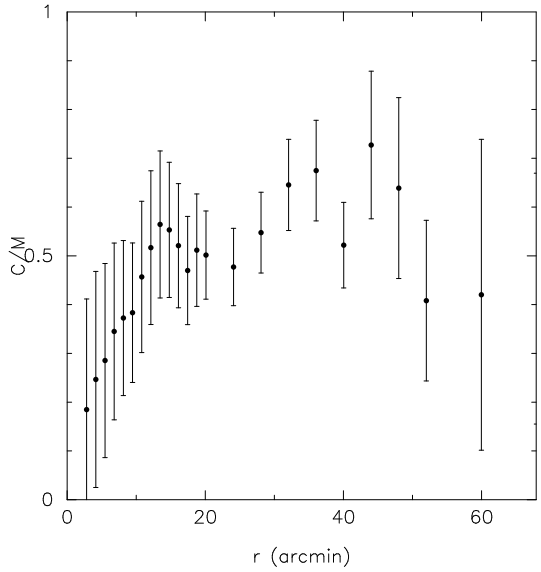


Fig. 17.— The C/M-star ratio as a function of galactocentric radius (note: 1 arcmin $\simeq$ 0.25 kpc at a distance modulus of 24.64).

regions around the edge of the disk show C/M-ratios no higher than 0.4. It thus appears that the higher C/M-ratios are real. These regions could simply mark the outer reaches of spiral arms with lower metallicities. Both regions do have spiral arm structure within them. Figure 19 shows a CMD for a region located at the edge of the visible disk of M33. The stellar populations and features of the CMD in Figure 6 are still visible. However, the CMD does not show any significant morphological differences. A deeper survey is necessary to search for a distinctive stellar population in the region, that could consist of an old, low-luminousity stellar population.

The first panel in Figure 18 also shows that the C/M-ratio is a function of galactocentric radius. This gives the galaxy the appearance of being surrounded by a ring of material with a lower metallicity. It has recently been suggested that the Milky Way is also surrounded by a ring traced by stars of lower metallicitiy (Ibata et al. 2003). As suggested by Ibata et al. (2003), this feature could be extended spiral arm structure. In galaxy formation simulations the edge of the disk is expected to be young and contain metal poor gas (Navarro & Steinmetz 1997). In M33, the regions of low metallicity also correspond to the edge of the disk, as traced by C-star and MS-star populations. In the Milky Way, distinct spiral arm structure has been identified from 21-cm emission (Davies (1972), Ibata et al. (2003)). This similarity suggests that the Milky Way "ring" may be consistent with spiral arms and does not require tidal interaction of dwarf galaxies for its formation. We may be seeing the same effect here in M33.

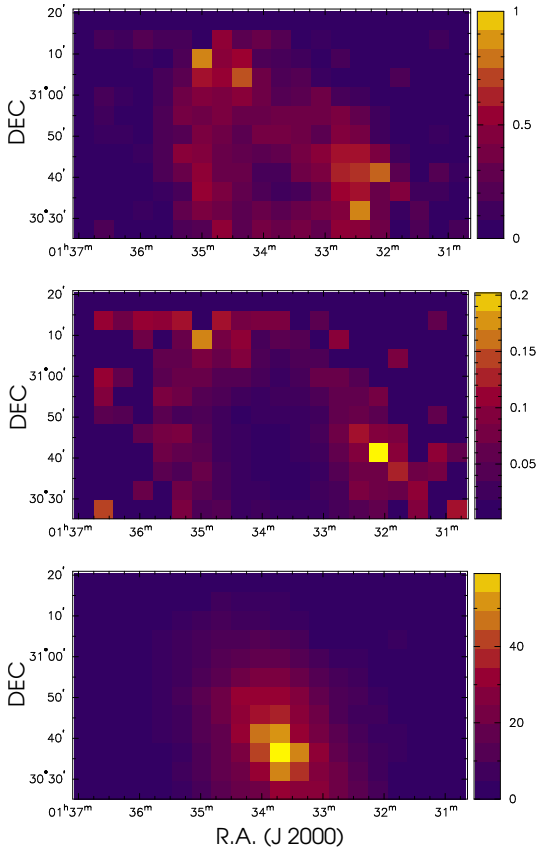


Fig. 18.— The top panel shows the spatial map of the C/M-star ratio. The middle panel shows the associated error in the C/M-star ratio and the bottom panel plots the signal-to-noise ratio.

### 4.6. C-star Luminosity Function

This study has identified 7936 C-stars and Figure 20 show the corresponding completeness corrected luminosity functions (LF) for V, I and bolometric magnitudes.

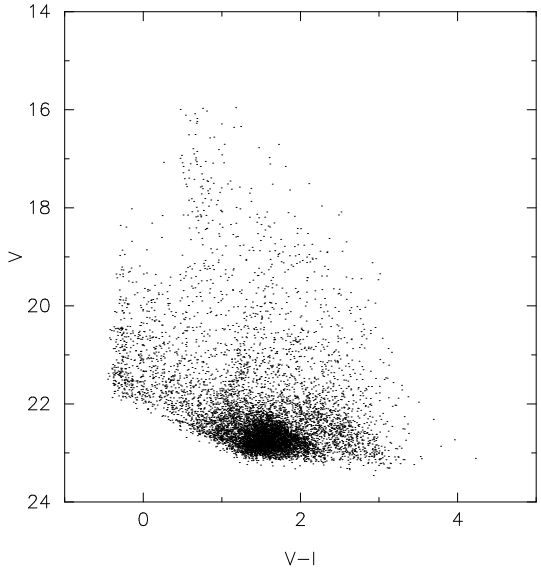


Fig. 19.— Colour-magnitude diagram for V versus V−I for a 10′ box centered at approximately $1^{\rm h}35.45^{\rm m}$ $+31°10'$, near the edge of M33's visible disk.

The LF is similar to those observed in other systems such as M31 and the SMC as shown in Groenewegen (2002). To calculate absolute bolometric magnitudes for the C-stars we used a distance modulus of 24.64 (Freedman et al. 1991) with the bolometric correction (BC) given by Bessell & Wood (1984) for M-stars.

$$M_{bol} = I + BC - 24.64$$
$$BC = 0.3 + 0.38(V-I) - 0.14(V-I)^2. \quad (2)$$

The C-star luminosity function (CSLF) has a narrow peak and thus has potential as a good distance indicator (Richer (1989), Groenewegen (2002)). The problem is disentangling the dependence of the peak magnitude of the CSLF on galactic properties such as metallicity or star formation history. Figure 8 of Groenewegen (2002) shows that the mean of the CSLF does not depend on [Fe/H], with most systems having a mean bolometric magnitude between -4 and -5. Discrepancies can be explained either through incompleteness of the CSLF at faint magnitudes causing the mean to be too bright, or the absence of an intermediate age population leaving only faint C-stars. In M33 the average bolometric magnitude is found to be $-4.2$ mag $\pm$ 0.1 which is similar to M31 and the SMC (both have $M_{\rm bol} = -4.3$). Because such diverse systems have similar C-star LFs, C-stars could be used as distance indicators.

## 5. Conclusions

Using a four-band photometric system, the AGB stars in the nearby spiral galaxy M33 were classified into C and M-star types. The photometry catalogue allowed an examination of the different stellar populations of M33. M33 has a large number of MS OB stars being produced by current star formation. The extent of the disk and spiral arm structure was shown through examination of the spatial distributions of MS and SGB-stars. The AGB population, being older, is dispersed and only tenuously trails the spiral arm structure The distribution of the AGB stars revealed no smaller galactic companions, such as those found in the local environments of M31 or the Milky Way.

Using colour-colour diagrams, the C-star and M-star populations were used to map the C/M-star ratio. The C/M-star ratio is known to trace metallicity, and the C/M-ratio profile and C/M-star map were produced. The C/M-star profile shows a metallicity gradient dependent on galactocentric radius. The profile was found to flatten at the same radius at which the radial-velocity profile also flattens. These results are consistent with viscous-disk formation models where the metallicity gradient becomes flattened in the outer part of the disk as material originating at different initial radii become mixed.

The C/M-star map shows the outer parts of M33's galactic disk to be metal poor. This can give the appearance to an observer located inside the galaxy that they are surrounded by a ring of metal poor material. The C/M-star map also shows two regions with an enhanced C/M-star ratio. These regions may be a natural occurrence at the end of a spiral arm, or may trace a different underlying population. These regions will require deep follow-up photometric surveys to examine the stellar populations in order to explain the implied lower metallicity in these regions.

This research has made use of the NASA/IPAC Extragalactic Database (NED) which is operated by the Jet Propulsion Laboratory, California Institute of Technology, under contract with the National Aeronautics and Space Administration.

## REFERENCES

Aaronson, M. Da Costa, G.S. Hartigan, P. Mould, J.R. Norris, J. Stockman, H.S. 1984, ApJ, 277, L9

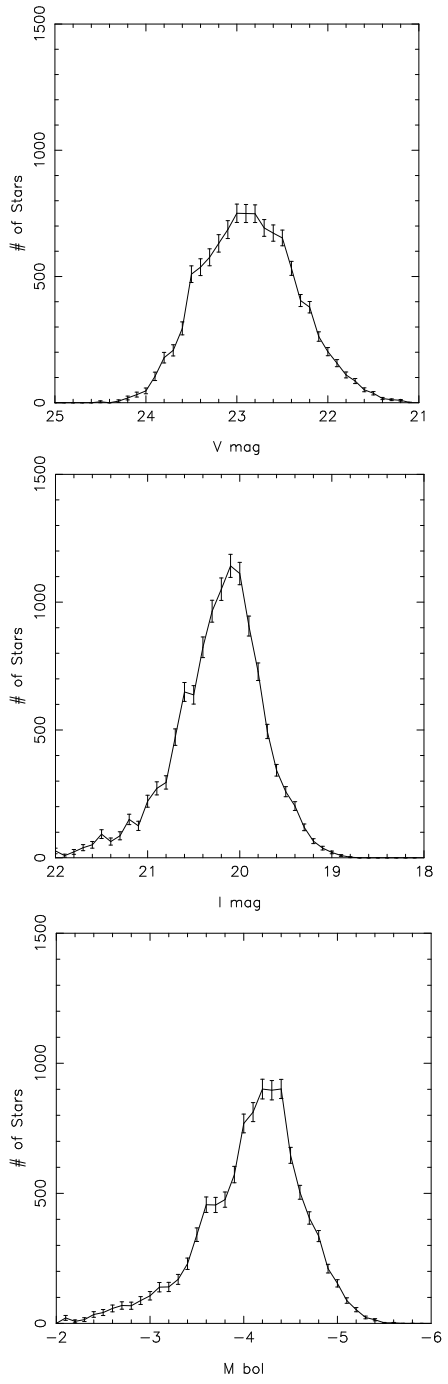


Fig. 20.— Magnitude distribution of C-stars for V-filter, I-filter and bolometric magnitudes.

Aaronson, M. Olszewski, E.W. 1987, AJ, 94, 657

Albert, L. Demers, S. Kunkel, W.E. 2000, AJ, 119, 2780

Bessell, M.S. Wood, P.R. 1984, PASP, 96, 247

Blanco, V.M. Blanco, B.M. McCarthy, F.M. 1980, ApJ, 242, 938

Blanco, V.M. McCarthy, M.F. 1983, AJ, 88, 1442

Block, D.L., Freeman, K.C., Jarrett, T.H., Puerari, I., Worthey, G., Combes, F. & Groess, R. 2004, astro-ph/0406485

Brewer, J.P. Richer, H.B. Crabtree,D.R. 1995, AJ, 109, 2480

Brewer, J.P. Richer, H.B. Crabtree, D.R. 1996, AJ, 112, 491

Cook, K.H. Aaronson, M. Norris, J. 1986, ApJ, 305, 634

Corbelli, E. Salucci, P. 2000, MNRAS, 311, 441

Davies, R.D. 1972, MNRAS, 160, 381

Dekel, A. Silk, J. 1986, ApJ, 303, 39

Durrell, P.R. Harris, W.E. Pritchet, C.J. 2001 AJ, 121, 2557

Ferguson, A.M.N. Irwin, M.J., Ibata, R.A. Lewis, G.F. Tanvir, N.R. 2002, AJ, 124, 1452

Freedman, W.L. Wilson, C.D. Madore, B.F. 1991, ApJ, 372, 455

Girardi, L. Bressan, A. Bertelli, G. Chiosi, C. 2000, A&AS, 141, 371

Green, P.J. 1992, PASP, 104, 977

Groenewegen, M.A.T. 2002, astro-ph/0208449

Hayashi, E. Navarro, J.F. 2002, in *American Astronomical Society Meeting*, 201

Hudon, J.D. Richer, H.B. Pritchet, C.J. Crabtree, D. Christian, C.A. Jones, J. 1989, AJ, 98, 1265

Ibata, R.A. Irwin, M.J. Lewis, G.F. Ferguson, A.M.N. Tanvir, N. 2003, MNRAS, 340,L21

Klypin, A. Kravtsov, A.V. Valenzuela, O. Prada, F. 1999, ApJ, 522, 82

Krisciunas, K. 1990, PASP, 102, 1052

Letarte, B. Demers, S. Battinelli, P. Kunkel, W.E. 2002, AJ, 123, 832

Macri, L.M. Stanek, K.Z. Sasselov, D.D. Krockenberger, M. Kaluzny, J. AJ, 121, 861

Moore, B. Ghigna, S. Governato, F. Lake, G. Quinn, T. Stadel J., Tozzi, P. 1999, ApJ, 524, L19

Mouhcine, M. Lançon, A. 2003, MNRAS, 338, 572

Mould, J. Aaronson, M. 1986, ApJ, 303, 10

Navarro, J.F. Steinmetz, M. 1997, ApJ, 478, 13

Newberg, H.J. Yanny, B. Rockosi, C. Grebel, E.K. Rix, H. Brinkmann, J. Csabai, I. Hennessy, G. Hindsley, R.B. Ibata, R. Ivezić, Z. Lamb, D. Nash, E.T. Odenkirchen, M. Rave, H.A. Schneider, D.P. Smith, J.A. Stolte, A. York D.G. 2002, ApJ, 569, 245

Nowotny, W. Kerschbaum, F. Schwarz, H.E. & Olofsson, H. 2001, A&A, 367, 557

Odenkirchen, M. Grebel, E.K. Rockosi, C.M. Dehnen, W. Ibata, R. Rix, H. Stolte, A. Wolf, C. Anderson, J.E. Bahcall, N.A. Brinkmann, J. Csabai, I. Hennessy, G. Hindsley, R.B. Ivezić, Ž. Lupton, R.H. Munn, J.A. Pier, J.R. Stoughton, C. York, D.G. 2001, ApJ, 548, L165

Pritchet, C.J. Schade, D. Richer, H.B. Crabtree, D. Yee, H.K.C. 1987, ApJ, 323, 79

Richer, H.B. 1989, in Evolution of peculiar red giant stars; Proceedings of the 106th IAU Colloquium, Bloomington, IN, July 27-29, 1988 Cambridge University Press, 1989, p. 35-50.

Richer, H.B. Crabtree, D.R. Pritchet, C.J. 1984, ApJ, 287, 138

Richer, H.B. Pritchet, C.J. Crabtree, D.R. 1985a, ApJ, 298, 240

Richer, H.B. Crabtree, D.R. 1985b, ApJ, 298, L13

Richer, H.B. Crabtree, D.R. Pritchet, C.J. 1990, ApJ, 355, 448

Sommer-Larsen, J. Yoshii, Y. 1990, MNRAS, 243, 468

Stetson, P.B. 1987, PASP, 99, 191

Stetson, P.B. 1994, PASP, 106, 250

Vilchez, J.M. Pagel, B.E.J. Diaz, A.I. Terlevich, E. Edmunds, M.G. 1988, MNRAS, 235, 633

Vivas, A.K. Zinn, R. 2003, Mem. Soc. Astron. Italiana, 74, 928

White, S.D.M. Rees, M.J. 1978, MNRAS, 183, 341

Zaritsky, D. 1992, ApJ, 390,L73

This 2-column preprint was prepared with the AAS LaTeX macros v5.2.

Table 1: Filters used in the Four Band Photometry System

| Filter | Central Wavelength (nm) | Bandwidth (nm) | Max. Trans. (%) |
|---|---|---|---|
| Mould V | 537.4 | 97.4 | 94 |
| Mould I | 822.3 | 216.4 | 91 |
| TiO | 777.7 | 18.4 | 92 |
| CN | 812.0 | 16.1 | 95 |

Table 2: Target list

| Field ID | R.A. | DEC |
|---|---|---|
| M33-1 | $1^{h}35^{m}24^{s}$ | $+31°06'30''$ |
| M33-2 | $1^{h}32^{m}18^{s}$ | $+31°06'30''$ |
| M33-3 | $1^{h}35^{m}23^{s}$ | $+30°39'30''$ |
| M33-4 | $1^{h}32^{m}18^{s}$ | $+30°39'30''$ |

Table 3: Observation Log

| Date | Target | Filter | Exp. (s) | FWHM ($''$) | Airmass |
|---|---|---|---|---|---|
| Oct 30, 1999 | M33-3 | V | 3 × 400 | 0.7, 0.7, 0.7 | 1.20, 1.18, 1.16 |
| | M33-3 | I | 3 × 200 | 0.6, 0.6, 0.6 | 1.10, 1.09, 1.08 |
| | M33-4 | I | 3 × 200 | 0.6, 0.6, 0.6 | 1.07, 1.06, 1.06 |
| | M33-4 | V | 3 × 400 | 0.7, 0.7, 0.7 | 1.05, 1.05, 1.04 |
| | M33-1 | V | 3 × 400 | 0.6, 0.6, 0.6 | 1.03, 1.03, 1.03 |
| | M33-1 | I | 3 × 200 | 0.8, 0.8, 0.8 | 1.02, 1.02, 1.02 |
| | M33-2 | I | 3 × 200 | 0.8, 0.8, 0.8 | 1.02, 1.02, 1.02 |
| | M33-2 | V | 3 × 400 | 0.9, 0.9, 0.9 | 1.03, 1.03, 1.04 |
| | Sky Flat | V | 30, 21, 15, 11, 6, 5, 4 | – | – |
| Oct 31, 1999 | Sky Flat | I | 4, 5, 7, 9, 12, 17, 24 | – | – |
| | Bias | – | 4 × 0 | – | – |
| Dec 3, 2000 | M33-3 | TiO | 3 × 1000 | 0.6, 0.6, 0.6 | 1.07, 1.05, 1.04 |
| | M33-3 | CN | 3 × 1000 | 0.8, 0.8, 0.8 | 1.02, 1.02, 1.02 |
| | M33-4 | CN | 3 × 1000 | 0.5, 0.5, 0.6 | 1.04, 1.05, 1.08 |
| | M33-4 | TiO | 3 × 1000 | 0.7, 0.7, 0.9 | 1.12, 1.16, 1.21 |
| | M33-1 | TiO | 3 × 1200 | 1.0, 1.3, 1,3 | 1.29, 1.38, 1.49 |
| | Sky Flat | TiO | 3, 7, 4 | – | – |
| | Bias | – | 0 | – | – |
| Dec 4, 2000 | Sky Flat | CN | 6 × 5,7 | – | – |
| | Sky Flat | TiO | 2 × 12, 2 x 20, 30 | – | – |
| | Sky Flat | CN | 40, 60, 100, 140, 200 | – | – |
| | Bias | – | 0 | – | – |
| | M33-1 | CN | 3 × 1000 | 0.7, 0.6, 0.7 | 1.04, 1.06, 1.08 |
| | M33-1 | TiO | 3 × 1000 | 0.7, 0.7, 0.7 | 1.13, 1.17, 1.22 |
| | M33-2 | TiO | 3 × 1000 | 0.7, 0.8, 0.8 | 1.33, 1.42, 1.52 |
| | M33-2 | CN | 3 × 1000 | 0.8, 0.8, 0.8 | 1.72, 1.90, 2.12 |
| | Bias | – | 6 × 0 | – | – |

Table 4: Object Catalog for M33 (abridged)

| Star ID | R.A. | DEC | V | $\sigma_V$ | I | $\sigma_I$ | CN | $\sigma_{CN}$ | TiO | $\sigma_{TiO}$ | $\chi$ | Sharp |
|---|---|---|---|---|---|---|---|---|---|---|---|---|
| 1 | 1 31 04.68 | 30 52 07.70 | 15.8437 | 0.0423 | 15.1750 | 0.0118 | 9.4495 | 0.0079 | 9.5432 | 0.0088 | 2.8480 | 0.0670 |
| 2 | 1 30 45.71 | 30 45 01.00 | 16.7190 | 0.0231 | 99.9990 | 9.9990 | 10.0849 | 0.0366 | 10.3589 | 0.0140 | 4.7347 | 0.1315 |
| 3 | 1 30 45.15 | 30 51 37.80 | 16.5790 | 0.0048 | 16.0423 | 0.0095 | 10.3286 | 0.0040 | 10.2939 | 0.0036 | 1.4807 | 0.1440 |
| 4 | 1 31 03.82 | 30 51 36.90 | 17.4459 | 0.0576 | 99.9990 | 9.9990 | 10.6256 | 0.1168 | 10.3792 | 0.1184 | 14.6062 | 0.9263 |
| 5 | 1 31 07.73 | 30 49 09.80 | 17.1538 | 0.1146 | 16.0570 | 0.0768 | 10.2046 | 0.1594 | 10.2802 | 0.0882 | 18.9920 | 2.0965 |

## TABLE CAPTIONS

Table 1. Filters: Column (1) names the filter, column (2) gives the central wavelength in nanometres, column (3) gives the filter width in nanometres and column (4) gives the maximum transmission as a percentage.

Table 2. Target List: Column (1) gives the field ID, columns (2) and (3) gives the right accension and declination in J2000 co-ordinates.

Table 3. Observation log: Column (1) gives the date of the observation, column(2) gives the target field or type of calibration image, column (3) gives the filter used, column (4) gives the number of exposures and exposure time in seconds and column (5) gives the average full-width-half-maximum (FWHM) of stars on each frame in arc seconds.

Table 4. Object catalogue: column (1) gives the star ID, column (2) and column (3) give the right accension and declination in J2000 co-ordinates, columns (4), (6), (8), (10) give the V, I, CN and TiO magitudes and columns (5), (7), (9), (11) give the associated photometric error returned by ALLSTAR. Columns (12) and (13) give the Chi-squared and Sharp values for the PSF fit from DAOPhot.